Patient-specific fluid–structure simulations of anomalous aortic origin of right coronary arteries

Check for updates

Michael X. Jiang, MD, MEng,[a,b] Muhammad O. Khan, PhD,[c] Joanna Ghobrial, MD,[d] Ian S. Rogers, MD,[e] Gosta B. Pettersson, MD, PhD,[f] Eugene H. Blackstone, MD,[f,g] and Alison L. Marsden, PhD[c]

ABSTRACT

Objectives: Anomalous aortic origin of the right coronary artery (AAORCA) may cause ischemia and sudden death. However, the specific anatomic indications for surgery are unclear, so dobutamine-stress instantaneous wave-free ratio (iFR) is increasingly used. Meanwhile, advances in fluid–structure interaction (FSI) modeling can simulate the pulsatile hemodynamics and tissue deformation. We sought to evaluate the feasibility of simulating the resting and dobutamine-stress iFR in AAORCA using patient-specific FSI models and to visualize the mechanism of ischemia within the intramural geometry and associated lumen narrowing.

Methods: We developed 6 patient-specific FSI models of AAORCA using SimVascular software. Three-dimensional geometries were segmented from coronary computed tomography angiography. Vascular outlets were coupled to lumped-parameter networks that included dynamic compression of the coronary microvasculature and were tuned to each patient's vitals and cardiac output.

Results: All cases were interarterial, and 5 of 6 had an intramural course. Measured iFRs ranged from 0.95 to 0.98 at rest and 0.80 to 0.95 under dobutamine stress. After we tuned the distal coronary resistances to achieve a stress flow rate triple that at rest, the simulations adequately matched the measured iFRs (r = 0.85, root-mean-square error = 0.04). The intramural lumen remained narrowed with simulated stress and resulted in lower iFRs without needing external compression from the pulmonary root.

Conclusions: Patient-specific FSI modeling of AAORCA is a promising, noninvasive method to assess the iFR reduction caused by intramural geometries and inform surgical intervention. However, the models' sensitivity to distal coronary resistance suggests that quantitative stress-perfusion imaging may augment virtual and invasive iFR studies. (JTCVS Techniques 2022;13:144-62)
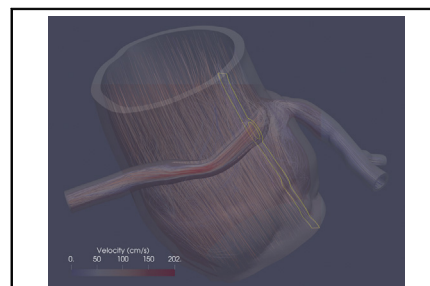
Computational model of anomalous intramural coronary tissue deformation and blood flow.

CENTRAL MESSAGE

Patient-specific computational fluid–structure interaction modeling is a promising noninvasive tool to quantify the hemodynamic impact of the anomalous aortic origin of the right coronary artery.

PERSPECTIVE

Instantaneous wave-free ratio directly measures ischemia due to the anomalous aortic origin of a right coronary artery at stress. To noninvasively acquire the same values from computed tomography, we developed novel computational models of vascular wall deformation and perfusion. The simulation accuracy demonstrated the potential for fluid–structure interaction modeling to guide surgical management.

Abbreviations and Acronyms

3D	=	3-dimensional
AAOCA	=	anomalous aortic origin of a coronary artery
AAORCA	=	anomalous aortic origin of a right coronary artery
CTA	=	computed tomography angiography
FFR	=	fractional flow reserve
FSI	=	fluid–structure interaction
iFR	=	instantaneous wave-free ratio
RMSE	=	root-mean-square error

▶ Video clip is available online.

Anomalous aortic origin of a coronary artery (AAOCA) is a congenital malformation in which the coronary artery arises from the aorta outside of the normal coronary sinus of Valsalva.[1,2] It is the second-leading cause of sudden death in otherwise-healthy youth.[3,4] Present in 0.1% to 1.5% of the general population, most AAOCA cases are asymptomatic and presumed to be benign.[1,2]

Previous AAOCA autopsies and registries found greater frequencies of ischemia and sudden death among certain anatomic variants.[4,5] Notably, the cumulative risk of sudden death for young athletes from 15 to 35 years of age is approximately 6.3% for the anomalous left main coronary artery and 0.2% for the anomalous right coronary artery.[2] Therefore, current guidelines recommend surgical repair of all anomalous *left main* coronary arteries but only anomalous *right* coronary arteries (AAORCA) in the presence of ischemia or other morphologic risk factors.[2,6] Greater-risk morphologic features visible on noninvasive imaging include a high ostial takeoff (above the sinutubular junction), slit-like orifice, interarterial course (passing between the great arteries), and intramural course (passing circumferentially within the aortic wall).[2,5] Despite these risk factors, many patients with AAOCA survive through late adulthood with an indeterminate ischemic burden and concomitant cardiovascular comorbidities.[7,8] Therefore, further risk stratification is necessary, especially for adults with AAORCA.

The controversy regarding treatment recommendations is complicated by the uncertainty about the exact mechanism of ischemia. Although a narrowed ostium intuitively restricts blood flow, the effect of the proximal course anatomy is less clear. Some believe that the great arteries compress the interarterial segment during exercise, whereas others doubt pulmonary artery pressures are sufficient.[2,9] Alternatively, the expanding aorta may push the interarterial coronary against the pulmonary root stemming from the cardiac fibrous skeleton.[8] As the aorta distends outward, the wall is also stretched thinner, potentially narrowing the cross-sectional area of the intramural course. Understanding the exact mechanism is critical to guide the extent of surgical intramural unroofing and predict the potential benefit of pulmonary artery translocation for interarterial coronaries.[2,10]

To guide clinical management, some centers use invasive pressure catheters to measure intracoronary hemodynamics at rest and with dobutamine stress to simulate exercise.[11,12] Similar to fractional flow reserve (FFR), instantaneous wave-free ratio (iFR) measures the averaged poststenotic pressure as a fraction of the upstream reference but focuses only on the wave-free period, the portion of diastole when the coronary microcirculation resistance is minimized.[13] Based on stable coronary artery disease trials, iFR ≤ 0.89 is often considered hemodynamically significant, at rest or dobutamine stress, indicating a need for intervention.[14,15] However, these invasive procedures are expensive, difficult with a tight ostium, and carry a small risk of coronary dissection and bleeding.

One noninvasive option is using coronary computed tomography angiography (CTA) for patient-specific computational fluid dynamics modeling, which has simulated the FFR in atherosclerotic coronary artery disease and the hemodynamics affecting bypass graft survival.[16,17] More recently, computational fluid dynamics has also been used to model the FFR and hemodynamics in AAOCA, but such methods have yet to be validated with direct measurements for anomalous coronaries.[18-20] Also, computational fluid dynamics modeling fails to simulate the coronary lumen compression that may occur during exercise. Meanwhile, advancements in fluid–structure interaction (FSI) modeling enable simultaneous modeling of blood flow and tissue deformation, but to our knowledge, this approach has not been applied to AAOCA.

We hypothesized that patient-specific FSI simulations of AAORCA yield iFRs similar to the invasively measured values in the cardiac catheterization lab during rest and dobutamine-stress. If accurate, such a model of AAORCA may noninvasively quantify the ischemic burden in individual patients and guide surgical management if necessary.

METHODS

Patients and Clinical Characteristics

Cleveland Clinic's institutional review board approved the use of data for this clinical cohort study, with patient consent waived (study number 17-1087, approved August 15, 2017, expiration date August 14, 2021). We identified 6 patients with AAORCA with an available coronary CTA who underwent a dobutamine-stress iFR cardiac catheterization between April 2018 and May 2019. Baseline characteristics (including demographics, coronary anatomy, and noninvasive stress tests) were abstracted from the patients' electronic medical records (Table 1). Coronary anatomy was determined based on operative reports (when available) and expert

TABLE 1. Baseline patient characteristics

ID	Age, y	Sex	Symptoms	Noninvasive stress	Comorbidities	% Diameter CAD stenosis (LMCA/LAD/ LCx/RCA)	Inter-arterial	Intra-mural
1	45	F	Angina, dyspnea, palpitation	Equivocal (ECG)	Asthma, obesity, anxiety	0/30/0/0	Yes	No
2	60	M	Atypical angina	Normal (echocardiogram, ECG)	None	0/0/0/0	Yes	Yes
3	63	M	Atypical angina, dyspnea	Normal (ECG, PET)	HTN	0/0/0/0	Yes	Yes
4	24	F	Atypical angina, dyspnea, palpitation	None	Arrhythmia, asthma, LAD myocardial bridge	0/0/0/0	Yes	Yes
5	42	F	Syncope	Equivocal (ECG)	Arrhythmia	0/0/0/0	Yes	Yes
6	53	F	NSTEMI, angina, dyspnea	Normal (ECG, PET)	HTN, HLD, anxiety	0/0/0/0	Yes	Yes
Average ± SD	48 ± 14					0/5/0/0		

Patient characteristics at the time of iFR study. Stress tests results were recorded normal, ischemic, or equivocal. Inducible ischemia was based on stress electrocardiography, echocardiography, or nuclear perfusion imaging. *CAD*, Coronary artery disease; *LMCA*, left main coronary artery; *LAD*, left anterior descending coronary artery; *LCx*, left circumflex coronary artery; *RCA*, right coronary artery; *F*, female; *ECG*, electrocardiogram; *M*, male; *PET*, positron emission tomography; *HTN*, hypertension; *NSTEMI*, non-ST-elevation myocardial infarction; *HLD*, hyperlipidemia; *SD*, standard deviation.

review of the coronary CTA. Noninvasive stress tests included electrocardiography, echocardiography, single-photon emission computed tomography, and positron emission tomography. For each modality, we categorized the results as normal, equivocal, or definite for myocardial ischemia. Electrocardiography results were classified as indicative of ischemia if the ST changes met diagnostic criteria. Similarly, we classified the imaging studies as indicative of ischemia if a wall motion abnormality or perfusion defect correlated with the territory supplied by the AAOCA. Otherwise, abnormal results were defined as equivocal.

Patient-Specific FSI Modeling

We constructed the patient-specific FSI models in SimVascular, an open-source software platform for modeling cardiovascular blood flow.[21] Specifically, we used the svFSI solver, which implements an arbitrary Lagrangian–Eulerian method to simultaneously calculate fluid flow and tissue deformation.[21] Material characteristics such as the densities, blood viscosity, and tissue elasticity properties were the same for all patients and described in greater detail in the Appendix 1.

Baseline geometric models of the lumen were segmented from each patient's coronary CTA (Figure 1). The vascular walls were offset from the lumen of the aortic root and coronary arteries by their corresponding thicknesses. The 3-dimensional (3D) models were then discretized into millions of tetrahedral elements to achieve adequate spatial resolution and accuracy.

Next, we assigned the boundary conditions, mathematical properties that defined the forces and movement at surfaces. The inlets and outlets were fixed in space whereas the external surfaces freely moved. The aortic fluid inlet was a time-dependent pressure source scaled to the patient's blood pressure and heart rates (Figure E1). For the fluid outlets, the same hemodynamic parameters, along with stroke volume, scaled each component in the lumped-parameter network, which mathematically modeled the downstream physiology. Importantly, the coronary lumped-parameter model included a dynamic pressure source (representing the ventricular compression of the microvasculature). We also simulated low- and high-exercise conditions that targeted volumetric flows at 2 and 3 times resting values, respectively, consistent with previous coronary computational fluid

dynamics models.[22] We also incorporated the internal stresses within the vascular wall using a previously described prestress modeling process.[23,24] The method and justification of scaling all parameters at rest and stress is detailed in Appendix 1.

Ultimately, the svFSI solver calculated the corresponding tissue deformation and blood flow over 5 cardiac cycles. The resulting pressure ratio between the aortic inlet and coronary outlet during the wave-free period was calculated as specified by the iFR_MATLAB algorithm (Figure 2).[13]

Sensitivity Analysis: Mesh Resolution and Pulmonary Root Forces

We verified mesh convergence by doubling the resolution of the solid and fluid domain for one model. As an exploratory effort, we added the mechanical effects of the adjacent pulmonary root in another patient. The external surface contacting the pulmonary root was assigned a Robin-type boundary condition, which acted as a spring pushing back against the interarterial coronary. Additional details of the mesh generation and Robin-type boundary condition are described in Appendix 1.

Statistics

Patient clinical characteristics were summarized with averages and standard deviations. Accuracy of FSI-simulated iFR compared with invasively measured values was evaluated with the root-mean-square error (RMSE), and the Bland–Altman plot with 95% confidence limits of the mean difference. We also reported the linear regression of the simulated iFR over the measured iFR and the corresponding Pearson's correlation coefficient, r. All analyses were completed in R, version 4.0.3 (R Core Team).[25]

RESULTS

Patient Characteristics and Association With Measured iFR

The 6 patients in this adult AAORCA cohort had a mean age of 48 ± 14 years (range 24-63 years). Most were female
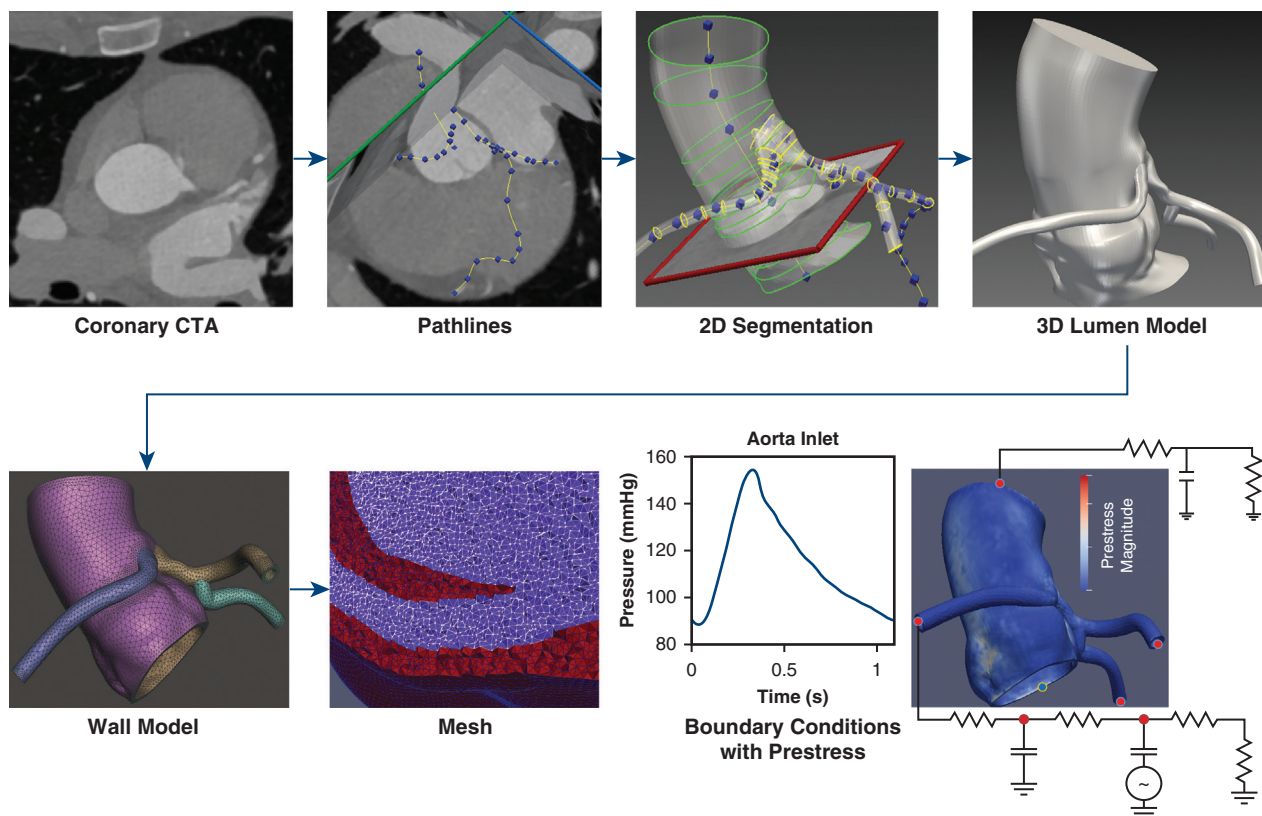
FIGURE 1. Fluid–structure interaction (FSI) modeling pipeline with SimVascular. Computed tomography angiographies (*CTAs*) were segmented by first drawing pathlines and 2-dimensional cross-sections to generate the 3-dimensional lumen model. Vessel walls came from offsetting the lumen by set thicknesses. Both the fluid and solid domains were meshed with local refinement around the proximal anomalous coronary. The simulated prestress within the solid tissue was added as a boundary condition along with the inlet pressure and outlet lumped-parameter networks.

(4/6, 67%). All had atypical cardiac symptoms leading to coronary imaging that diagnosed the AAOCRA. Each anomalous coronary had an interarterial course and arose leftward of the left-right commissure near the sinotubular junction. All but one had an intramural course. There was no atherosclerotic coronary artery disease ≥30% stenosis or any definitive ischemia on noninvasive stress tests. Therefore, the recommendation for surgical intervention for these patients was difficult, prompting further iFR assessment. Dobutamine-stress lowered the average iFR from 0.96 ± 0.02 (range 0.95-0.98) at rest to 0.87 ± 0.06 (range 0.80-0.95). Individual iFR measurements and hemodynamic parameters are summarized in Table 2.

For this clinically significant range of dobutamine-stress iFR, we assessed whether any of the easily measured input hemodynamic parameters for the FSI models independently predicted the measured iFR. Neither blood pressures, heart rates, nor cardiac outputs at stress correlated with the measured stress iFR (Figure E2). Unsurprisingly, the patient with the greatest iFRs at both rest and stress was the only one lacking an intramural course.

Of the 4 patients who had a dobutamine-stress iFR less than 0.89, 3 underwent coronary unroofing. One surgical patient is still undergoing postoperative evaluation for ischemia as of the last follow-up in 2021. The other 2 had chest pain resolve after surgery and dobutamine-stress iFR improvements from 0.80 to 0.93 and 0.84 to 0.91. The patient with a dobutamine-stress iFR 0.83 had a systolic pressure of 240 mm Hg during the test and was managed medically for the abnormal hypertensive response first.

FSI-Simulated iFR Accuracy

Under resting conditions, the simulated iFR reasonably matched the measured iFR (RMSE = 0.02). For the dobutamine-stress condition, the simulated iFR was more accurate after targeting a multiplier of 3 times rather than 2 times the resting flow (RMSE = 0.05 vs 0.08, respectively) (Figure E3). The lower flow tended to underestimate the iFR reduction (such that the simulated iFR was greater than that measured). The combined iFRs at rest and stress demonstrated a moderately strong linear correlation between the simulated and measured iFRs (r = 0.85, RMSE = 0.04, Figure 3). Bland–Altman analysis demonstrated moderate agreement between the measured and simulated iFR within differences ≤0.05, except for one outlier in which the simulated dobutamine-stress iFR was 0.09 lower than the measured value (Figure 4).
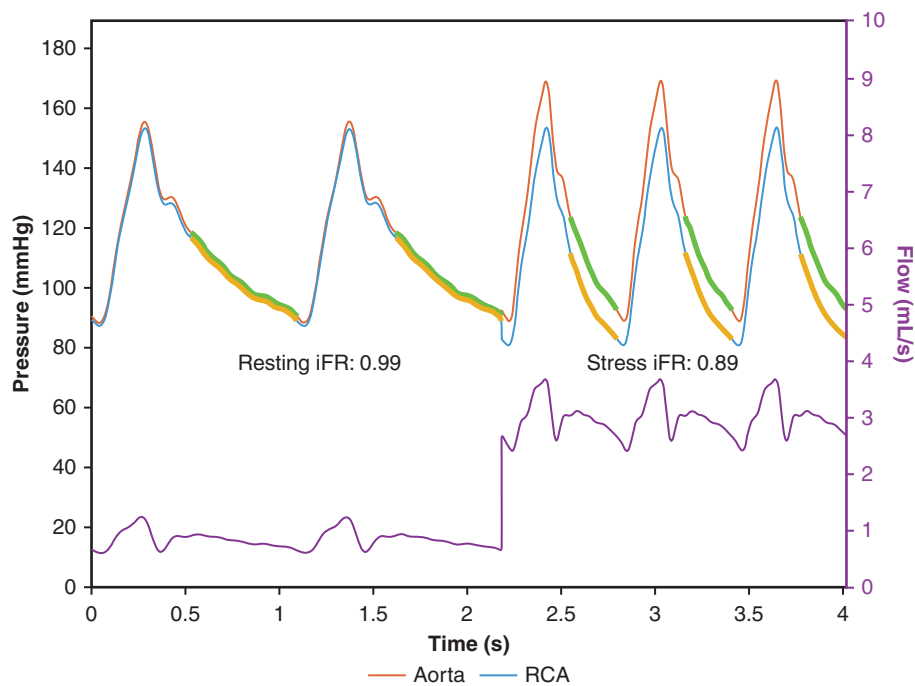
FIGURE 2. Representative flows and pressures in aorta and right coronary artery (*RCA*). The aortic (*red*) and RCA (*blue*) pressures were similar at rest but separated with dobutamine stress, during which the flow (*purple*) through the RCA increased to 3 times the resting rate. The iFR was calculated during the wave-free period as the mean ratio between the RCA (*orange*) and aorta (*green*) pressures. *iFR*, Instantaneous wave-free ratio.

In addition to the numeric iFR values, the hemodynamic waveforms from which they were derived also appeared reliable. After a few initial cardiac cycles to wash out transients, the pressures and flows converged to a periodic steady-state during which we calculate the iFR (Figure E4). The flow through the anomalous right coronary had a physiologic bimodal velocity waveform, whereas the left coronary flow peaked only in diastole as expected. After

dobutamine stress, all the anomalous right coronaries developed substantial pressure drops relative to the aorta, especially during diastole.

Our sensitivity analyses verified that the mesh resolution and pulmonary root had minimal effects on the results. After the total number of elements was doubled, the simulated pressures and flows were nearly identical with less than a 1% change in iFR (Figure E5). Adding the pulmonary

TABLE 2. Measured hemodynamic parameters

Patient number	Heart rate, bpm	Blood pressure, mm Hg	Cardiac output, L/min	Measured iFR	Simulated iFR
Rest					
1	95	137/94	5.9	0.98	0.99
2	58	140/85	4.3	0.97	0.97
3	53	140/78	4.3	0.95	0.99
4	100	91/61	4.9	0.95	0.98
5	99	114/61	4.5	0.98	0.97
6	76	122/63	4.9	0.95	0.96
Average ± SD	80 ± 21	124/74 ± 19/14	4.8 ± 0.6	0.96 ± 0.02	0.98 ± 0.01
Stress					
1	142	155/94	N/A	0.95	0.98
2	110	240/150	N/A	0.83	0.87
3	134	142/134	11.0	0.84	0.89
4	162	103/68	N/A	0.86	0.85
5	151	146/74	N/A	0.95	0.86
6	164	138/85	10.2	0.80	0.75
Average ± SD	144 ± 20	154/101 ± 46/34	10.6 ± 0.6	0.87 ± 0.06	0.87 ± 0.07

The invasively measured iFR value, our primary outcome, is listed with the patient-specific parameters in the fluid–structure interaction models for the resting and dobutamine stress conditions. These parameters included the heart rate, blood pressures (systolic/diastolic), and cardiac output. *iFR*, Instantaneous wave-free ratio; *SD*, standard deviation; *N/A*, not available.
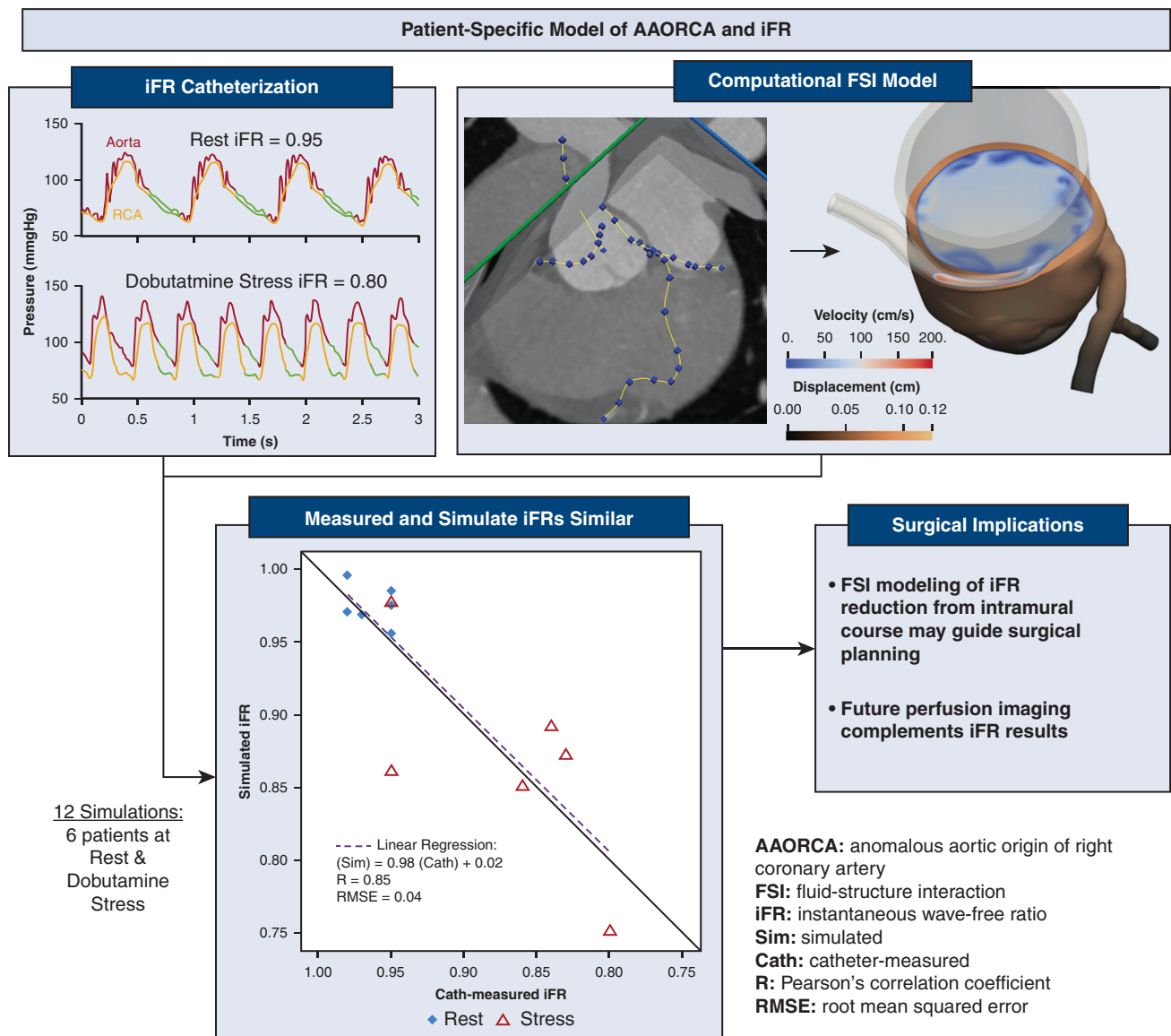
FIGURE 3. Correlation between simulated and measured iFR. To quantify the ischemic burden from the anomalous aortic origin of a right coronary artery (*AAORCA*), we invasively measured the iFR at rest and dobutamine stress. We also computationally simulated the iFRs with fluid–structure interaction (*FSI*) models segmented from computed tomography. The strong correlation between measured and simulated iFRs suggests that noninvasive FSI modeling may accurately assess anomalous coronaries and guide surgical management. *iFR*, Instantaneous wave-free ratio; *RMSE*, root mean squared error.

root stiffness caused the contact surface displacement between the coronary and pulmonary artery to fall from 0.72 mm to 0.02 mm, but the iFR changed by less than 1% (Figure E6). The interarterial segment maintained the same cross-sectional shape but was prevented from translating outward by the pulmonary root.

DISCUSSION
FSI Model Accuracy and Uncertainty
For our primary outcome, we compared the resting and dobutamine-stress iFRs from the FSI simulations to those measured in the cardiac catheterization lab. The strong correlation (r = 0.85) in this study is somewhat greater than similarly reported results in successful clinical trials evaluating CTA-derived FFR for coronary artery disease patients with normal coronary origins (r = 0.80).[17] The FSI models also did not show significant systemic bias (eg, overestimation or underestimation) in iFR predictions during rest and stress. The overall error (RMSE = 0.04) was also small. For comparison, the beat-to-beat variation of iFR is about 0.01 to 0.02 and the mean difference between repeated measures of FFR has a standard deviation of 0.04.[26] Thus, our 6 AAORCA FSI models accurately simulated the iFR at rest and dobutamine stress using
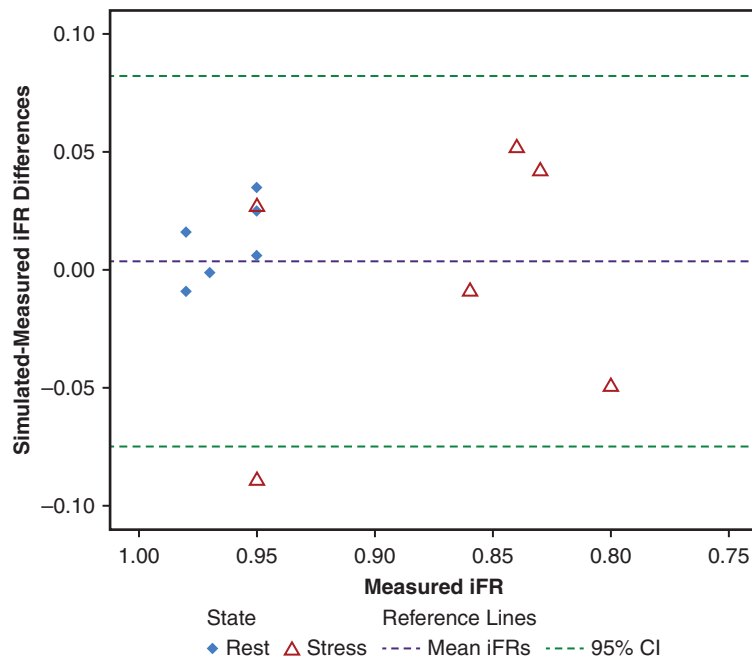
FIGURE 4. Bland–Altman plot analyzed the agreement between the FSI-simulated iFR to the iFR measured in the cardiac catheterization lab at both rest and dobutamine stress. The horizontal axis is the invasively measured reference iFR, and the vertical axis is the difference between that and the simulated iFR. *Horizontal reference lines* represent the mean difference and corresponding 95% confidence interval (*CI*). *FSI*, Fluid–structure interaction; *iFR*, instantaneous wave-free ratio.

only blood pressure, heart rate, and noninvasive imaging data.

We also assessed FSI simulation realism by examining the characteristic flow profile of the coronary and aortic outlets (Figure 3). The left coronary flows had a single peak during diastole (due to the systolic compression of the microvascular bed by the left ventricle).[27] In comparison, the ventricular compression of the right coronary system (which predominantly supplies the right ventricle) is weaker and permitted a greater systolic flow resulting in the characteristic bimodal flow waveform.

The accuracy of the simulated iFR also was not explained by the patient-specific hemodynamic input parameters alone. We suspected lower iFR values for patients with greater blood pressures, heart rates, and cardiac outputs, but none of these variables correlated with the measured iFR (Figure E2). Therefore, the full FSI simulation was necessary to integrate the patient-specific 3-dimensional geometry and hemodynamic measurements to accurately estimate the iFR.

The error between the simulated and measured iFR possibly arose from a variety of sources such as the 3-dimensional geometry, solid tissue properties, and boundary conditions. Image segmentation repeatability and intramural course interpretation were limited by the CTA resolution. The uncertainty from the distal coronary resistances was reflected by the different iFR results for the 2

volumetric flow rates for the stress condition. The more accurate results required raising the permitted coronary flow to 3 times the resting rate which is on the higher end of the expected stress-state coronary perfusion.[22] One recently published computational fluid model showed that the range of possible distal coronary resistances has a similar magnitude of FFR change as 70% narrowing of the proximal anomalous coronary.[28] Sensitivity to distal coronary resistances also highlights iFR's potential underappreciation of hemodynamic severity of AAOCA in the setting of microvascular disease.[15] To improve the model accuracy and assess microvascular dysfunction, quantitative myocardial perfusion imaging with positron emission tomography or cardiac magnetic resonance imaging may be helpful.[11]

To systematically quantify the effects of input parameters uncertainty on the iFR results, several approaches for uncertainty quantification suitable for cardiovascular models are available. One FSI study of normal resting coronary flow found that the variables with the strongest influence were the inlet pressure and the intramyocardial pressure (contained within the coronary lumped-parameter model).[29] Coronary wall elasticity had a minimal effect such that one standard deviation change in elasticity resulted in less than a 1% change in coronary flow. Other analyses in rigid-wall computational fluid dynamics studies found significant sources of uncertainty in the coronary lumped-parameter network values, especially the microvascular

resistance.[19,30] Despite the various sources of input variability, the resulting hemodynamic output was acceptably accurate such that the FFR predicted by CTA-based computational fluid dynamics is approved in the United States and the United Kingdom to guide clinical management of coronary artery disease.[17] Although adequately accurate for coronaries with normal origins, the robustness of computation simulations has yet to be proven for anomalous coronaries.

Mechanism of Ischemia Revealed by FSI Simulation

Our FSI simulations, which omitted pulmonary artery effects, demonstrated that the iFR reduction can be accurately explained by the intramural geometry alone. We also observed that the intramural lumen was restricted from expanding during exercise (Video 1). During stress, the lower distal coronary resistance allowed for a higher flow through the anomalous coronary (with a relatively constant cross-section) resulting in a proportionally greater pressure drop and a lower iFR. Thus, these simulation results implicated the intramural course rather than the interarterial course as the cause of ischemia.

Other engineering models and imaging studies of AAOCA also point to a similar ischemia mechanism. Finite element analyses of the intramural course under constant pressure loads (without flow simulation) found that the intramural lumen expands less compared to normal-origin coronary arteries.[9,31] Meanwhile, computational fluid dynamics simulations with rigid geometries showed how the narrowed intramural course caused significant hemodynamic
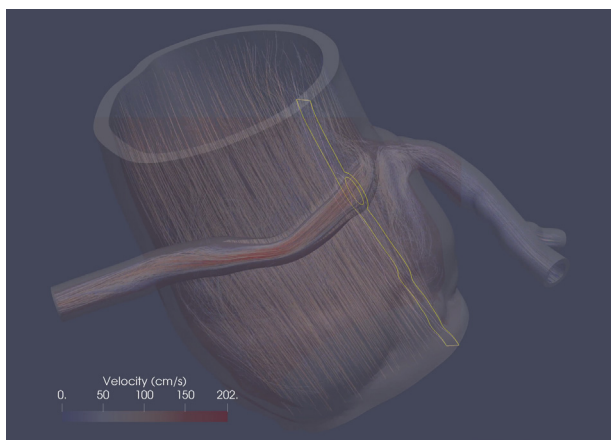

VIDEO 1. Representative patient-specific fluid–structure interaction simulation of anomalous aortic origin of a right coronary artery. Simulation with streamlines of blood flow through the aortic root and anomalous right coronary artery during dobutamine-stress shows flow acceleration in the intramural segment that remained narrow resulting in iFR reduction. The cross-section of the intramural course is outlined in *yellow*, and the reference resting diastolic geometry is outlined in *pink*. Video available at: https://www.jtcvs.org/article/S2666-2507(22)00129-8/fulltext.

abnormalities.[19,20,32] A 3D-printed model of an intramural AAORCA had an abnormally low FFR that normalized in a separate model of the postoperative geometry.[33] A cine CTA of an interarterial (but not intramural) anomalous left coronary found no luminal compression nor perfusion defect during dobutamine-stress.[34] In contrast, intravascular ultrasound of intramural left coronaries showed the intramural segments to be narrowed.[35] Interestingly, 1 of the 3 intravascular ultrasound cases showed a 10% worsening of the intramural stenosis after dobutamine-stress induction. Although the dobutamine-stress imaging studies were of the anomalous left coronary, the intramural course deformation is likely similar for AAORCA.

Although our FSI simulations implicated the intramural geometry as the primary culprit of stress-induced ischemia, the pulmonary root may still play a role in select interarterial cases. Previous AAOCA registries found associations between the interarterial course and ischemia or sudden death, but separating the intramural and interarterial effects through statistical models is difficult because the 2 features are highly correlated.[1,5] Additional FSI models of any ischemic interarterial cases without intramural courses could provide additional insights.

Implications for Surgical Intervention

Based on the atypical chest pain or indeterminate stress tests present in all patients within this cohort, the decision for surgical correction of the AAORCA was unclear. Using a dobutamine-stress iFR threshold of 0.89, 4 of 6 patients would have been recommended surgery. The FSI-simulated iFR results led to similar surgical recommendations except for 1 patient with a measured iFR of 0.95 but a simulated iFR of 0.86. The simulation would have recommended surgery whereas the invasively measured iFR would not have. Alternatively, this patient may have had undiagnosed microvascular dysfunction resulting in a greater measured iFR.[15] A second patient with a measured iFR of 0.85 had a simulated iFR of 0.89, which would have led to only a weak recommendation for surgical repair. Even with small differences in measured and simulated iFR, the discrepancy can still lead to divergent recommendations for surgical repair. This imperfect dichotomization also afflicts FFR-guided revascularization in coronary artery disease.[15] With further validation, patient-specific FSI models may become a noninvasive and cost-effective tool to recommend surgery versus medical observation.

Mechanistic insight from the FSI simulation also helps inform the surgical technique for AAOCA repair. Since the omission of the pulmonary root from these models still resulted in significantly low iFRs, pulmonary artery translocation likely would not have benefited these specific interarterial cases. Instead, unroofing, reimplantation, or neostium creation would be necessary to address the intramural course. None of the patients in this cohort were good

candidates for bypass grafting due to the absence of obstructive coronary artery disease, without which competitive flow through the native vessel would likely lead to early graft failure.[2] Had there been significant coronary artery disease, our simulation results could identify whether the ischemia was due to the anomalous origin or atherosclerotic stenosis. Determining the culprit lesion may improve the selection of surgical repair techniques. We can also preoperatively model the postoperative coronary anatomy and resulting hemodynamics to confirm that adequate coronary perfusion would be restored.[16,19]

Limitations

Although dobutamine-stress iFR is increasingly used to guide clinical management, the correlation between iFR and risk of major adverse cardiac events in anomalous coronaries has yet to be validated. Like noninvasive stress tests, iFR has traditionally been used to assess fixed atherosclerotic coronary artery disease.[14,15] That no patients in our cohort had clear signs of ischemia on nuclear perfusion imaging, despite suspicious symptoms, also underscores the limitations of noninvasive ischemia assessment in AAOCA. Patients with strong evidence of ischemia on noninvasive testing attributable to AAOCA would have undergone surgery without the need for further iFR testing. Thus, our study lacked patients with confirmed ischemia on noninvasive testing. With no single modality representing the gold standard, we were unable to calculate the sensitivity or specificity of our iFR results. Future studies comparing iFR with other ischemia testing modalities and clinical outcomes are necessary.

While our FSI simulations were more complete than previous AAOCA computational models, some aspects may have been oversimplified. For example, all but one case omitted the effects of the pulmonary root. Also, the solid tissue was modeled as a uniform isotropic material despite the frequent proximity of the stiff commissures and our intraoperative observation that the intramural course is often surrounded by more fibrotic tissue. Increasing the model complexity with different material properties may result in less reproducibility between model builders and increase uncertainty of results, but such advancements should be confirmed in future studies.[9]

Given the time-intensive manual 3-dimensional model construction process and significant computational costs of FSI simulations, the sample size of this study was limited to only 6 adult patients with AAORCA containing an interarterial course. To generalize the FSI modeling to all patients with AAOCA, stronger validation of accuracy and robustness is needed with and increased sample size that includes anomalous left coronaries, other morphologic variants, and children.

CONCLUSIONS

Patient-specific FSI modeling of iFR is a promising tool to noninvasively quantify the hemodynamic significance of AAORCA with dobutamine stress. Compression from the pulmonary root was unnecessary to achieve accurate iFR results, suggesting that the narrowed intramural course is a sufficient mechanism of ischemia. However, additional models incorporating the pulmonary root may be necessary to rule out ischemia due to the interarterial course for specific patients. Finally, the FSI model's sensitivity to the volumetric flow rate permitted by the distal coronary microvascular resistance suggests a future role for quantitative stress-perfusion imaging to complement iFR for risk stratification of AAOCA.

Conflict of Interest Statement

The authors reported no conflicts of interest.

The *Journal* policy requires editors and reviewers to disclose conflicts of interest and to decline handling or reviewing manuscripts for which they may have a conflict of interest. The editors and reviewers of this article have no conflicts of interest.

References

1. Cheezum MK, Liberthson RR, Shah NR, Villines TC, O'Gara PT, Landzberg MJ, et al. Anomalous aortic origin of a coronary artery from the inappropriate sinus of Valsalva. *J Am Coll Cardiol*. 2017;69:1592-608.
2. Brothers JA, Frommelt MA, Jaquiss RDB, Myerburg RJ, Fraser CD, Tweddell JS. Expert consensus guidelines: anomalous aortic origin of a coronary artery. *J Thorac Cardiovasc Surg*. 2017;153:1440-57.
3. Maron BJ, Doerer JJ, Haas TS, Tierney DM, Mueller FO. Sudden deaths in young competitive athletes. *Circulation*. 2009;119:1085-92.
4. Eckart RE, Shry EA, Burke AP, McNear JA, Appel DA, Castillo-Rojas LM, et al. Sudden death in young adults: an autopsy-based series of a population undergoing active surveillance. *J Am Coll Cardiol*. 2011;58:1254-61.
5. Jegatheeswaran A, Devlin PJ, McCrindle BW, Williams WG, Jacobs ML, Blackstone EH, et al. Features associated with myocardial ischemia in anomalous aortic origin of a coronary artery: a Congenital Heart Surgeons' Society study. *J Thorac Cardiovasc Surg*. 2019;158:822-34.e3.
6. Stout KK, Daniels CJ, Aboulhosn JA, Bozkurt B, Broberg CS, Colman JM, et al. 2018 AHA/ACC guideline for the management of adults with congenital heart disease: executive summary: a report of the American College of Cardiology/American Heart Association task force on clinical practice guidelines. *J Am Coll Cardiol*. 2019;73:1494-563.
7. Jiang MX, Blackstone EH, Karamlou T, Ghobrial J, Brinza EK, Haupt MJ, et al. Anomalous aortic origin of a coronary artery in adults. *Ann Thorac Surg*. 2021;112:1299-305.
8. Krasuski RA, Magyar D, Hart S, Kalahasti V, Lorber R, Hobbs R, et al. Long-term outcome and impact of surgery on adults with coronary arteries originating from the opposite coronary cusp. *Circulation*. 2011;123:154-62.
9. Lo Rito M, Romarowski RM, Rosato A, Pica S, Secchi F, Giamberti A, et al. Anomalous aortic origin of coronary artery biomechanical modeling: toward clinical application. *J Thorac Cardiovasc Surg*. 2021;161:191-201.e1.

10. Mainwaring RD, Murphy DJ, Rogers IS, Chan FP, Petrossian E, Palmon M, et al. Surgical repair of 115 patients with anomalous aortic origin of a coronary artery from a single institution. *World J Pediatr Congenit Heart Surg*. 2016;7:353-9.

11. Molossi S, Martínez-Bravo LE, Mery CM. Anomalous aortic origin of a coronary artery. *Methodist DeBakey Cardiovasc J*. 2019;15:111121.

12. Lee SE, Yu CW, Park K, Park KW, Suh J-W, Cho Y-S, et al. Physiological and clinical relevance of anomalous right coronary artery originating from left sinus of Valsalva in adults. *Heart*. 2016;102:114-9.

13. van't Veer M, Pijls NHJ, Hennigan B, Watkins S, Ali ZA, De Bruyne B, et al. Comparison of different diastolic resting indexes to iFR: are they all equal? *J Am Coll Cardiol*. 2017;70:3088-96.

14. Doan TT, Wilkinson JC, Agrawal H, Molossi S, Alam M, Mery CM, et al. Instantaneous wave-free ratio (iFR) correlates with fractional flow reserve (FFR) assessment of coronary artery stenoses and myocardial bridges in children. *J Invasive Cardiol*. 2020;32:176-9.

15. Götberg M, Cook CM, Sen S, Nijjer S, Escaned J, Davies JE. The evolving future of instantaneous wave-free ratio and fractional flow reserve. *J Am Coll Cardiol*. 2017;70:1379-402.

16. Khan MO, Tran JS, Zhu H, Boyd J, Packard RRS, Karlsberg RP, et al. Low wall shear stress is associated with saphenous vein graft stenosis in patients with coronary artery bypass grafting. *J Cardiovasc Transl Res*. 2021;14:770-81.

17. Driessen RS, Danad I, Stuijfzand WJ, Raijmakers PG, Schumacher SP, van Diemen PA, et al. Comparison of coronary computed tomography angiography, fractional flow reserve, and perfusion imaging for ischemia diagnosis. *J Am Coll Cardiol*. 2019;73:161-73.

18. Adjedj J, Hyafil F, Halna du Fretay X, Dupouy P, Juliard JM, Ou P, et al. Physiological evaluation of anomalous aortic origin of a coronary artery using computed tomography–derived fractional flow reserve. *J Am Heart Assoc*. 2021;10:e018593.

19. Razavi A, Sachdeva S, Frommelt PC, LaDisa JF. Patient-specific numerical analysis of coronary flow in children with intramural anomalous aortic origin of coronary arteries. *Semin Thorac Cardiovasc Surg*. 2021;33:155-67.

20. Chidyagwai SG, Vardhan M, Kaplan M, Chamberlain R, Barker P, Randles A. Characterization of hemodynamics in anomalous aortic origin of coronary arteries using patient-specific modeling. *J Biomech*. 2022;132:110919.

21. Lan H, Updegrove A, Wilson NM, Maher GD, Shadden SC, Marsden AL. A Re-engineered software interface and workflow for the open-source SimVascular cardiovascular modeling package. *J Biomech Eng*. 2018;140:024501.

22. Kim HJ, Vignon-Clementel IE, Coogan JS, Figueroa CA, Jansen KE, Taylor CA. Patient-specific modeling of blood flow and pressure in human coronary arteries. *Ann Biomed Eng*. 2010;38:3195-209.

23. Bäumler K, Vedula V, Sailer AM, Seo J, Chiu P, Mistelbauer G, et al. Fluid–structure interaction simulations of patient-specific aortic dissection. *Biomech Model Mechanobiol*. 2020;19:1607-28.

24. Hsu M-C, Bazilevs Y. Blood vessel tissue prestress modeling for vascular fluid–structure interaction simulation. *Finite Elem Anal Des*. 2011;47:593-9.

25. R Core Team. *R: A Language and Environment for Statistical Computing*. R Foundation for Statistical Computing; 2020.

26. Sen S, Escaned J, Malik IS, Mikhail GW, Foale RA, Mila R, et al. Development and validation of a new adenosine-independent index of stenosis severity from coronary wave–intensity analysis: results of the ADVISE (Adenosine Vasodilator Independent Stenosis Evaluation) study. *J Am Coll Cardiol*. 2012;59:1392-402.

27. Sankaran S, Esmaily Moghadam M, Kahn AM, Tseng EE, Guccione JM, Marsden AL. Patient-specific multiscale modeling of blood flow for coronary artery bypass graft surgery. *Ann Biomed Eng*. 2012;40:2228-42.

28. Razavi A, Sachdeva S, Frommelt P, LaDisa J. Computational assessment of hemodynamic significance in patients with intramural anomalous aortic origin of the coronary artery using virtually derived fractional flow reserve and downstream microvascular resistance. *J Biomech Eng*. 2022;144:031005.

29. Seo J, Schiavazzi DE, Kahn AM, Marsden AL. The effects of clinically-derived parametric data uncertainty in patient-specific coronary simulations with deformable walls. *Int J Numer Methods Biomed Eng*. 2020;36:e3351.

30. Tran JS, Schiavazzi DE, Ramachandra AB, Kahn AM, Marsden AL. Automated tuning for parameter identification and uncertainty quantification in multi-scale coronary simulations. *Comput Fluids*. 2017;142:128-38.

31. Formato GM, Lo Rito M, Auricchio F, Frigiola A, Conti M. Aortic expansion induces lumen narrowing in anomalous coronary arteries: a parametric structural finite element analysis. *J Biomech Eng*. 2018;140:111008.

32. Rigatelli G, Zuin M, Galasso P, Carraro M, D'Elia K, Daniela L, et al. Mechanisms of myocardial ischemia inducing sudden cardiac death in athletes with anomalous coronary origin from the opposite sinus: insights from a computational fluid dynamic study. *Cardiovasc Revasc Med*. 2019;20:1112-6.

33. Hatoum H, Krishnamurthy R, Parthasarathy J, Flemister DC, Krull CM, Walter BA, et al. Flow dynamics in anomalous aortic origin of a coronary artery in children: importance of the intramural segment. *Semin Thorac Cardiovasc Surg*. 2022;34:226-35.

34. Linsen PVM, Kofflard MJM, Lam SW, Kock MCJM. First in humans: dobutamine stress cardiac computed tomography to evaluate dynamic compression of an anomalous left coronary artery. *Coron Artery Dis*. 2018;29:607-8.

35. Angelini P, Walmsley RP, Libreros A, Ott DA. Symptomatic anomalous origination of the left coronary artery from the opposite sinus of Valsalva. *Tex Heart Inst J*. 2006;33:171-9.

APPENDIX 1. FLUID–STRUCTURE INTERACTION (FSI) MODELING PROCESS

First, we identified the best diastolic phase (typically 75% R-R interval) of the patient's computed tomography angiography and imported the Digital Imaging and Communications in Medicine file into SimVascular, an open-source software platform for modeling blood flow through cardiovascular structures.[E1] The segmentation process for converting the image into a 3-dimensional (3D) model started with creating pathlines for the aorta and coronary arteries by stepping through the Digital Imaging and Communications in Medicine slices (Figure 1). Next, the 2-dimensional cross-sectional profiles of the vessel lumens were segmented along the previously set pathlines. For each set of 2-dimensional segmentation, we used a lofting procedure to generate the 3D models of the outlined lumen.

Creating the model for the vessel walls required us to use an additional application, MeshMixer (by Autodesk). To transfer the 3D geometries from SimVascular to MeshMixer, we exported the 3D models for the aorta and each coronary artery as separate STL files. After each anatomic component was imported into MeshMixer, we generated the walls for each vessel by offsetting the imported lumen outward with the "convert to solid" feature. We typically used a thickness of 1.7 mm for the aortic wall and 0.9 mm for the coronary wall thickness, average values found in the literature.[1-3] However, we sometimes adjusted the thickness to better approximate the patient-specific anatomy. If an intramural segment (as defined by the flattened lumen cross-section) is not fully covered by the aorta, the aortic wall was thickened. If the distal coronary wall collided with the aortic wall, the coronary wall was thinned. The pulmonary root also served as a reference geometry that limited coronary and aortic root thickness. We then used Boolean addition to merge offset surfaces and Boolean subtraction to cut out the lumens of all the vessels. The ends of each vessel were trimmed to an appropriate length before the entire surface was remeshed to optimize mesh quality. To generate the fluid domain, the internal surfaces of the solid domain were copied and the ends were capped. After optimizing the fluid mesh, geometries for both domains were exported back out of MeshMixer as new STL files.

The new fluid and solid geometries were then imported back into SimVascular to generate the final meshes. Volume mesh generation used the open-source TetGen package (while keeping the optimized surface mesh unchanged). Element sizes were selected such that all walls were at least 2 elements thick and lumen cross-sections were at least 5 elements wide, resulting in millions of elements in total. After multiple iterations of adjusting meshing parameters to optimize mesh quality, the completed surfaces and volumes were then exported out VTP and VTU files, respectively.

With the model geometries completed, we then set the mechanical properties and boundary conditions for the fluid domain. We treated the blood as a Newtonian fluid with a density of 1.04 g/cm^3 and a viscosity of 0.4 dynes/cm^2.[22] We applied a backflow stabilization coefficient of 0.3 to prevent divergence of the numerical solution due to backflow that otherwise may occur at large faces such as the aorta.[E2]

The fluid inlet was set as a Neumann boundary condition to match the aorta pressure waveform in the iFR measurements at rest and then at stress. To extract the iFR pressures, we used a plot digitizer tool and filtered the waveform with a Fast Fourier Transform algorithm to remove the high-frequency whip artifacts (from the catheter moving within the turbulent aortic root). We then used the filtered heart rate along with the systolic and diastolic pressure to transform a representative waveform of the aorta taken from published data (Figure E1).[E3] The pressures along the y-axis were transformed to match systolic and diastolic pressure targets. The time-domain was transformed linearly in 2 parts since the systolic period shortens proportionally less than the diastolic period with increasing heart rate. The systolic and diastolic periods were calculated from echo derived linear model of heart rate and systolic period (Equation 1).[E4,E5]

$$t_{systole} = 425 - 1.5 \, HR \qquad \text{Equation 1}$$

Where $t_{systole}$ is the systolic period in milliseconds and HR is the heart rate in beats per minute. The diastolic period filled in the remainder of the cardiac cycle time after the systolic period.

For all the fluid outlets, we defined the boundary condition as a lumped parameter network model and tuned the parameters to match patient-specific values (Table E1). The governing equations for the lumped-parameter models were defined in a separate module, cplBC, that communicates with the 3D solver, svFSI. Each component in the lumped-parameter network was set to achieve cardiac output based on the echo imaging report. However, only 2 of 6 patients in this cohort had stress echocardiography studies that reported cardiac output, both of which were 2.6 times higher during stress than at rest. The increase in cardiac output is consistent with previous dobutamine-stress positron emission tomography that showed myocardial perfusion to increase by a factor of 1.7 to 3.1 from the resting rate.[E6] Therefore, we ran separate simulations to target double and triple the resting cardiac output, similar to previously described coronary simulations of low and high levels of exercise.[22]

The aorta outlet was modeled with an RCR-type boundary condition (Figure E7). The total resistance was split such that 9% was assigned to the proximal resistance and 91% was assigned to the distal resistance (representative

of a healthy patient).[22] The capacitance was also accordingly set to 0.001 cm^5/dyne. The governing equations for the aorta's lumped-parameter model are provided below, where Q_{ao} is the flow out the aorta, Pao is the aorta outlet pressure (averaged over the face of the 3D domain), P_d is the distal aorta pressure, P_{cvp} is the central venous pressure, R_p is the proximal resistance, R_d is the distal resistance, and C is the capacitance.

$$\frac{dP_d}{dt} = \frac{1}{C}\left(Q_{ao} - \frac{P_d - P_{cvp}}{R_d}\right) \qquad \text{Equation 2}$$

$$\frac{dP_{ao}}{dt} = Q_{ao} \times R_p + P_d \qquad \text{Equation 3}$$

The coronary outlets were assigned a coronary-type boundary condition with an intramyocardial pressure source which simulated the backpressure generated by the ventricular contraction around the microvascular coronary bed (Figure E8). The aforementioned governing equations for the coronary boundary conditions were adopted from Sankaran and colleagues[27] (Equations 4-6). The pressures (P) at each node corresponded with the aorta outlet (ao), arteriole (a), microcirculation (micro), and central venous pressure (cvp). The resistances (R) corresponded with those in coronary arteries (a), arterioles (a-micro), venules (v-micro), and veins (v). Finally, the model contained capacitive components (C) that represented the arterial capacitance (a) and microcirculatory capacitance (im).

$$P_{ao} = Q_{cor} \times R_a + P_a \qquad \text{Equation 4}$$

$$\frac{dP_a}{dt} = \frac{1}{C_a}\left(Q_{cor} - \frac{P_a - P_{micro}}{R_{a-micro}}\right) \qquad \text{Equation 5}$$

$$\frac{dP_{micro}}{dt} = \frac{1}{C_{im}}\left(\frac{P_a - P_{micro}}{R_{a-micro}} - \frac{P_{micro} - P_{cvp}}{R_{v-micro} + R_v}\right) + \frac{dP_{im}}{dt}$$
$$\text{Equation 6}$$

The total coronary resistances were calculated to achieve a mean flow that is proportional to the cardiac output. We assumed that 4% to 5% of cardiac output flows through the coronary arteries based on myocardial perfusion studies.[E7] We then assigned 30% of the coronary flow to the right coronary artery based on Doppler measurements and estimations from myocardial mass perfused by each coronary.[E8,E9] The remaining coronary flow was split between the left anterior descending and circumflex in a 60:40 ratio. These ratios between these resistances were held constant between rest and stress

simulations because experimental studies found a similar fractional flow rate in each state.[E6]

However, the ratio of resistive components within each lumped-parameter model changed with exercise following previous simulation studies.[22] At rest, the ratios were 0.32:0.52:0.16 for the proximal (Ra), intramyocardial (Ra-micro), and distal resistances (Rv-micro + Rv), respectively. At stress, this ratio changed to 0.55: 0.25:0.2: to account for the drop in microvascular resistance during exercise.

The capacitances also changed with exercise. At rest, we started with a total capacitance for the left coronaries of 3.6×10^{-5} cm^5/dyne, split in a 0.11:0.89 ratio for the proximal (Ca) and intramyocardial (Cim) capacitances.[22] For the right coronary at rest, the total capacitance was set to 2.5×10^{-5} cm^5/dyne with the same ratio between components. At stress, all capacitances were scaled proportionally with the cardiac output, to accommodate the increased flows and maintain physiologic flow waveforms.

The intramyocardial source was equal to the left ventricular pressure multiplied by a scaling factor—0.5 for the right coronary artery and 1.5 for the left coronary arteries.[22] This pressure source led to the characteristic biphasic flow for the right coronary and predominantly diastolic flow in the left coronary (Figure E4). The left ventricular pressure waveform was generated by scaling a representative waveform to the patients' measured arterial pressures (similar to the method for generating the aorta inlet pressure waveform). It was scaled such that the minimum pressure stayed constant (4 mm Hg) and the left ventricular pressure crossed the aorta shortly after the start of systole. The segment of the left ventricular pressures greater than the aortic pressures was scaled proportionally with the aortic pulse pressure.

With the parameters for the fluid domain set, we turned to set the boundary condition and constitutive properties for the solid tissue. The cut ends of the solid vessels were fixed in space as a Dirichlet boundary condition. The external surface was permitted to move freely as a Neumann boundary condition in which no pressure was applied to the outside surface. The internal surface was coupled to the interface surface in the fluid domain. For the aorta and coronary constitutive properties, we chose to use a neo-Hookean model for its simplicity and accuracy in modeling the mechanical behavior of other aorta simulations.[23,E10] The parameters of the neo-Hookean model were fit to the linearly approximated Young's modulus of the aortic root under physiologic blood pressure. Since the coronary arose from near the sinotubular junction, we utilized a weighted average of several estimates from the literature such that both the ascending aorta and aortic sinus stiffness had equal weight. After aggregating the material properties, we set our model's elasticity modulus (E) to be 1.5×10^7 dynes/

cm^2 (or 1.5 MPa), a poison ratio (ν) of 0.49, and a density of 1.2 g/cm^3.[E11-E13] These material properties, corresponded with Lamé's first parameter (λ) and shear modulus (G), according to the following equations.[E14]

$$G = \frac{E}{2(1+\nu)} \qquad \text{Equation 7}$$

$$\lambda = \frac{E\nu}{(1+\nu)(1-2\nu)} \qquad \text{Equation 8}$$

For one case, we ran an additional simulation with a Robin-type boundary condition applied to the external surface of the anomalous coronary contacting with the pulmonary root. This Robin-type boundary condition consisted of 2 parameters (ks = 8e^7 N/m^3, c = 0), based upon prior external tissue support simulations of the aorta.[23,E10]

Since the solid tissue also was under a load at rest, we solved for the internal stresses and applied it as a prestress for the FSI simulation.[23,24] The prestress process started with calculating the traction forces between the fluid and solid domain at rest. The traction was simulated by modeling the flow through the fluid domain corresponding with the pressures and flow rates at 75% R-R interval at rest. This traction file was converted from a VTU to a VTP file, representing just the forces at the fluid surface acting upon the solid domain. Next, the surface traction was applied as a boundary condition to the inner wall of the solid. To generate the prestress tensor, svFSI simulated the necessary internal stresses for all the surfaces in the solid domain to have minimal displacement. The result was applied as a prestress to the final FSI simulation, along with the velocity and pressure fields (from the traction calculation solution) as starting internal state conditions.

Finally, the FSI simulation was solved using svFSI over a maximum temporal step size of 1 millisecond at rest and 0.5 milliseconds at stress, over at least 5 cardiac cycles. The resulting pressures and volumetric flow rates at all the inlets and outlets were written to a data file which we then analyzed within MATLAB (MathWorks). The iFR was calculated as the ratio between the aorta inlet and coronary outlet during the wave-free period as specified by the iFR_MATLAB algorithm detailed by Van't Veer and colleagues (Figure 2).[13] The full 3D hemodynamics and tissue deformation results were visualized and analyzed within ParaView (Kitware, Inc).

E-References

E1. Updegrove A, Wilson NM, Merkow J, Lan H, Marsden AL, Shadden SC. Sim-Vascular: an open source pipeline for cardiovascular simulation. *Ann Biomed Eng*. 2017;45:525-41.

E2. Moghadam ME, Bazilevs Y, Hsia T-Y, Vignon-Clementel IE, Marsden AL. Modeling of Congenital Hearts Alliance (MOCHA). A comparison of outlet boundary treatments for prevention of backflow divergence with relevance to blood flow simulations. *Comput Mech*. 2011;48:277-91.

E3. Fuster V, Harrington R, Narula J, Eapen Z. *Hurst's the Heart*. In: *Two-Volume Set*. 14th ed. McGraw-Hill Education/Medical; 2017.

E4. Bombardini T, Gemignani V, Bianchini E, Venneri L, Petersen C, Pasanisi E, et al. Diastolic time–frequency relation in the stress echo lab: filling timing and flow at different heart rates. *Cardiovasc Ultrasound*. 2008;6:15.

E5. Cui W, Roberson DA, Chen Z, Madronero LF, Cuneo BF. Systolic and diastolic time intervals measured from Doppler tissue imaging: normal values and Z-score tables, and effects of age, heart rate, and body surface area. *J Am Soc Echocardiogr*. 2008;21:361-70.

E6. Krivokapich J, Czernin J, Schelbert HR. Dobutamine positron emission tomography: absolute quantitation of rest and dobutamine myocardial blood flow and correlation with cardiac work and percent diameter stenosis in patients with and without coronary artery disease. *J Am Coll Cardiol*. 1996;28:565-72.

E7. Hall JE. Muscle blood flow and cardiac output during exercise; the coronary circulation and ischemic heart disease. In: *Guyton and Hall Textbook of Medical Physiology*. Elsevier; 2016:259-70.

E8. Ofili EO, Labovitz AJ, Kern MJ. Coronary flow velocity dynamics in normal and diseased arteries. *Am J Cardiol*. 1993;71:D3-9.

E9. Kurata A, Kono A, Sakamoto T, Kido T, Mochizuki T, Higashino H, et al. Quantification of the myocardial area at risk using coronary CT angiography and Voronoi algorithm-based myocardial segmentation. *Eur Radiol*. 2015;25:49-57.

E10. Moireau P, Xiao N, Astorino M, Figueroa CA, Chapelle D, Taylor CA, et al. External tissue support and fluid–structure simulation in blood flows. *Biomech Model Mechanobiol*. 2012;11:1-18.

E11. Azadani AN, Chitsaz S, Matthews PB, Jaussaud N, Leung J, Tsinman T, et al. Comparison of mechanical properties of human ascending aorta and aortic sinuses. *Ann Thorac Surg*. 2012;93:87-94.

E12. Martin C, Pham T, Sun W. Significant differences in the material properties between aged human and porcine aortic tissues. *Eur J Cardiothorac Surg*. 2011;40:28-34.

E13. Mookhoek A, Krishnan K, Chitsaz S, Kuang H, Ge L, Schoof PH, et al. Biomechanics of failed pulmonary autografts compared to native aortic roots. *Ann Thorac Surg*. 2017;103:1482-8.

E14. Howell P, Kozyreff G, Ockendon J. Nonlinear elasticity. In: *Applied Solid Mechanics*. Cambridge University Press; 2008:215-44.
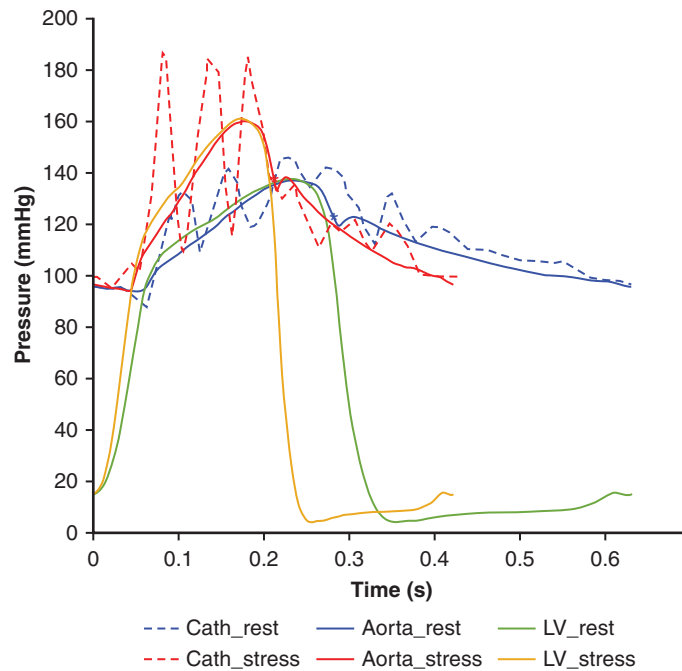
FIGURE E1. Simulation boundary condition with transformed pressure waveforms. Representative pressures measured by cardiac catheterization (*dotted lines*) had high-frequency whip artifacts. The raw waveforms were filtered and scaled to match the patient's blood pressures and heart rates at rest and stress as boundary condition inputs (*solid lines*) for the fluid–structure interaction models. Pressures shown at rest included the raw catheter measurements in the aorta (Cath_rest) and the simulated values for the aorta (Aorta_rest) and left ventricle (LV_rest). The same waveforms are shown for the stress conditions, respectively (Cath_stress, Aorta_stress, LV_stress).
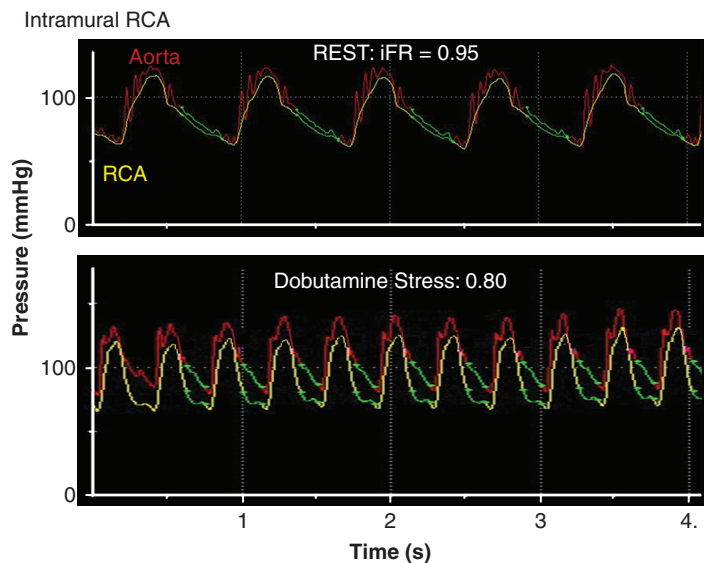
FIGURE E2. Association between measured dobutamine-stress iFR and each patient-specific input for the FSI model. No significant correlation was observed between the dobutamine-stress iFR and any of the patient-specific factors: blood pressures (BP; systolic and diastolic), heart rate, and cardiac output. Cardiac output at stress was modeled as either 2 or 3 times the cardiac output at rest. The *dotted trendline* represents the least-square regression. *RCA,* Right coronary artery; *iFR,* instantaneous wave-free ratio; *FSI,* fluid–structure interaction.
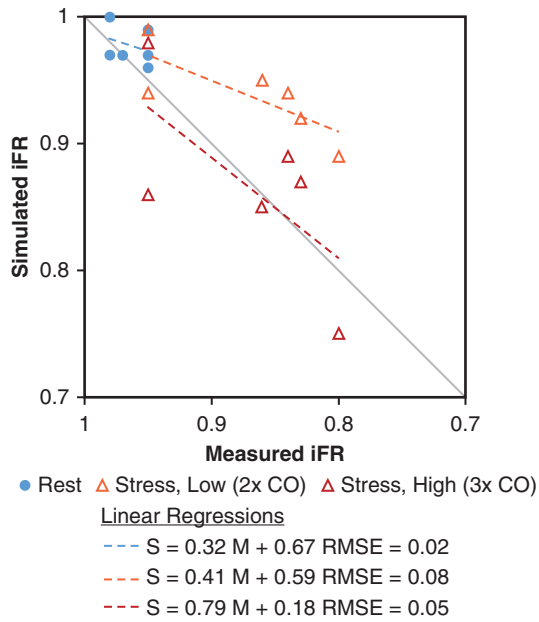
FIGURE E3. Correlation between FSI-simulated and measured iFR stratified by physiologic stress level. The iFR was simulated by the FSI model of AAORCA at rest and 2 stress conditions, one with 2 times the resting cardiac output ($2 \times CO$) and another with 3 times the resting cardiac output ($3 \times CO$). At rest, the FSI-simulated and measured iFR correlated closely, with a root mean square error (*RMSE*) of only 0.02. For the stress conditions, the higher cardiac output achieved a greater iFR reduction in the anomalous right coronary and matched the invasively measured iFR more closely (RMSE 0.05 vs 0.05). The *solid diagonal gray line* represents the ideal perfect correlation and the *dotted colored lines* represent the linear regressions corresponding to each of the stress levels. *FSI*, Fluid–structure interaction; *iFR*, instantaneous wave-free ratio; *AAORCA*, anomalous aortic origin of a right coronary artery; *S*, simulated iFR; *M*, measured iFR.
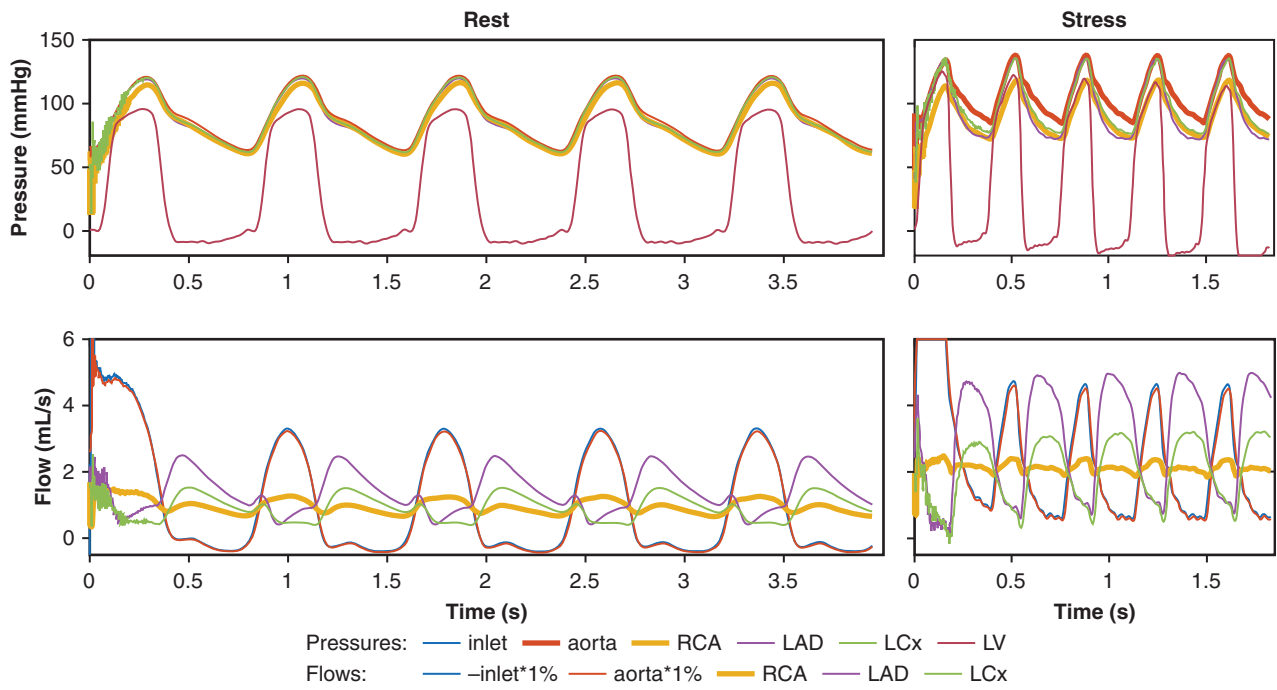
FIGURE E4. FSI-simulated pressure and flow rates. Representative simulation depicting pressures and flow rate converging to periodic steady-state within 5 cardiac cycles at rest and dobutamine stress. Pressures and flows shown included the inlet, aorta, right coronary artery (*RCA*), left anterior descending (*LAD*), and left circumflex (*LCx*). Pressure also included the left ventricle (*LV*). The flow rates for the inlet and aorta were scaled down to 1%.
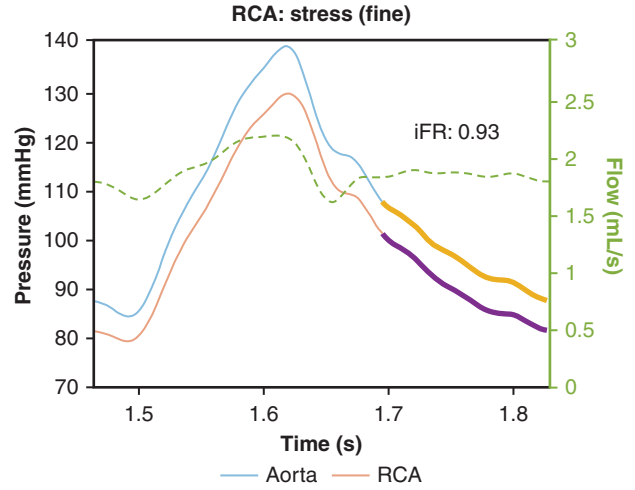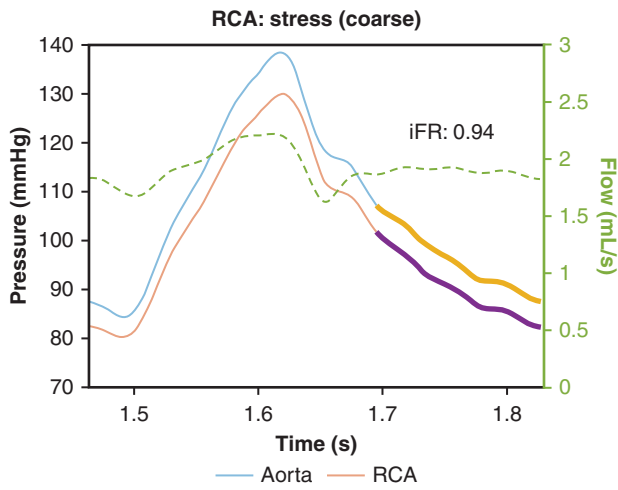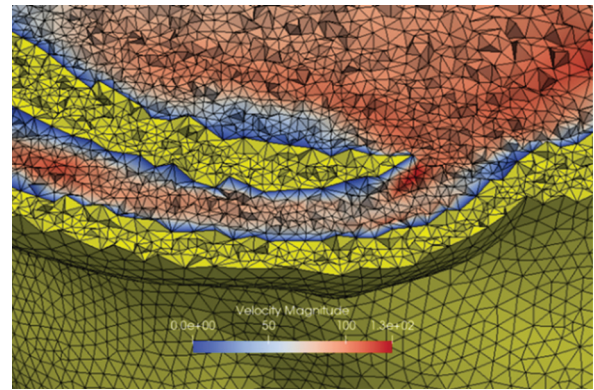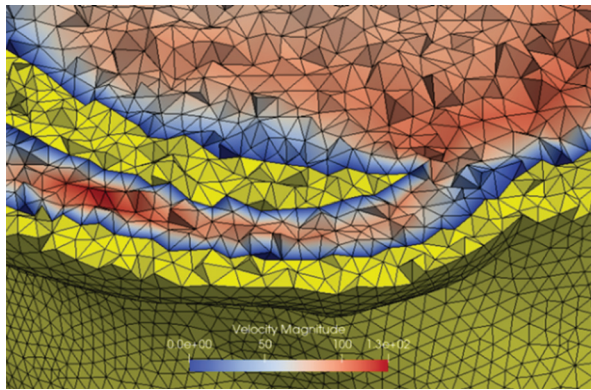
FIGURE E5. Mesh convergence on hemodynamic parameters. Representative example of an FSI simulation of an anomalous RCA under dobutamine. The total element count increased from 1.4 to 3.1 million, and the resolution across the short-axis of the intramural course increased from 4 to 7 elements wide. The different mesh resolutions yielded minimal change to the flow rates (*dotted*), pressures (*thin*), and wave-free period pressures (*thick*). *FSI*, Fluid–structure interaction; *RCA*, right coronary artery; *iFR*, instantaneous wave-free ratio.
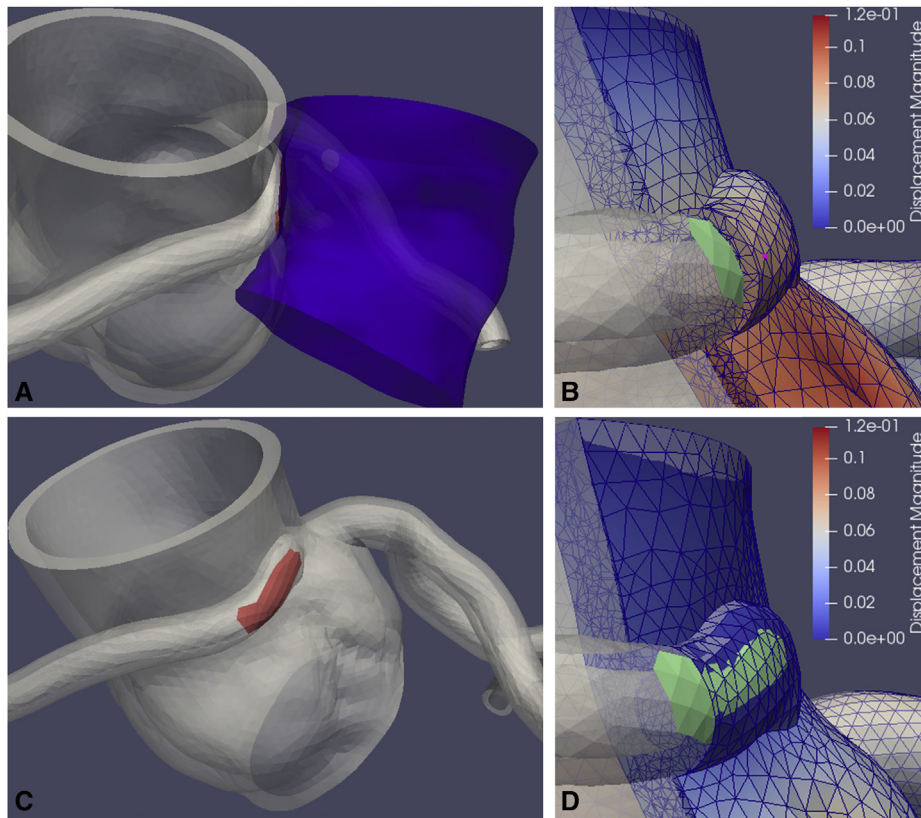
FIGURE E6. External compression from the pulmonary root. A and B, Pulmonary root (*violet*), pushing against the anomalous right coronary artery, was modeled as a Robin boundary condition applied to the contact surface (*red*). C, The displacement of the coronary artery external surface, relative to the original nondisplaced surface (*green*), exceeded 0.7 mm. D, After the stiffness of the pulmonary root was applied as a spring-like Robin boundary condition, the displacement decreased to less than 0.02 mm while the cross-sectional area of the intramural course and iFR remained the same. *iFR*, Instantaneous wave-free ratio.
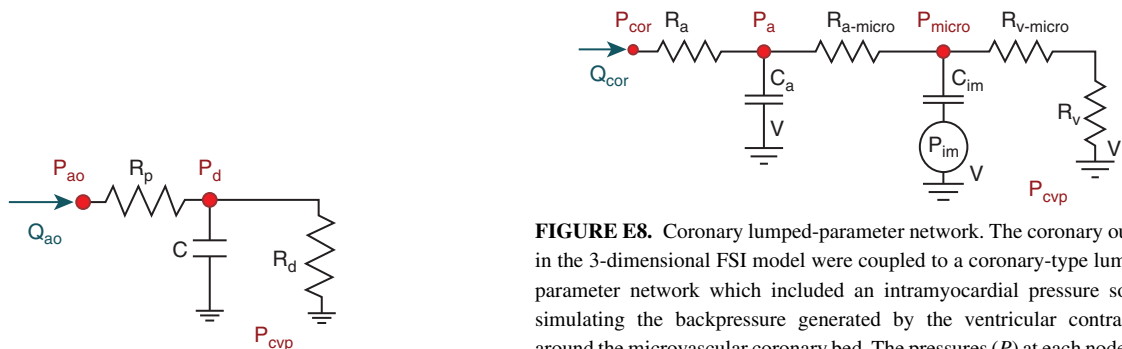

FIGURE E7. Aorta lumped-parameter network. A 3-element Windkessel lumped-parameter network was coupled to the aorta outlet of the 3D FSI model. Q is the flow out the aorta, P_{ao} is the aorta outlet, P_d is the distal aorta pressure, P_{cvp} is the central venous pressure, R_p is the proximal resistance, R_d is the distal resistance, and C is the capacitance. *FSI*, Fluid–structure interaction.

FIGURE E8. Coronary lumped-parameter network. The coronary outlets in the 3-dimensional FSI model were coupled to a coronary-type lumped-parameter network which included an intramyocardial pressure source simulating the backpressure generated by the ventricular contraction around the microvascular coronary bed. The pressures (*P*) at each node corresponded with the coronary outlet (*cor*), arteriole (*a*), microcirculation (*micro*), and central venous pressure (*cvp*). The resistances (*R*) corresponded with those in coronary arteries (*a*), arterioles (*a-micro*), venules (*v-micro*), and veins (*v*). The capacitive components (*C*) represented those for the coronary arterioles (*a*) and intramyocardial microvasculature (*im*). *FSI*, Fluid–structure interaction.

TABLE E1. Patient-specific parameters for inlet pressures and outlet lumped-parameter network models

Parameter	Rest	Stress
Aorta blood pressures	Cath	Cath
Cardiac output (CO)	Echo	$[2\text{-}3] \times CO_{rest}$
Aorta		
R_a:R_d	9:91	20:80
C (cm^5/dyne)	0.001	0.001
Coronary		
R_a:$R_{a\text{-micro}}$:$R_{v\text{-micro}} + R_v$	32:52:16	55:25:20
C_a:C_{im}	0.11:0.89	0.11:0.89
C_{RCA}, cm^5/dyne	2.5×10^{-5}	$\propto$ CO
C_{LAD}, cm^5/dyne	2.2×10^{-5}	$\propto$ CO
C_{LCx}, cm^5/dyne	1.4×10^{-5}	$\propto$ CO

Patient-specific aortic pressures originated from the iFR measurements at rest and stress. The target cardiac output (CO) from resting cardiac output (COrest) was doubled or tripled to approximate the stress condition. The remainder of the parameters were based on ratios from previously published coronary simulations. *Cath*, Cardiac catheterization; *echo*, echocardiography; *Ra:Rd*, proximal to distal aortic resistance ratio; *Ra:Ra-micro:Rv-micro + Rv*, coronary arteriole to microvascular to venule resistance ratios; *Ca:Cim*, coronary arteriole to intramyocardial capacitance ratios; C_{RCA}, C_{LAD}, C_{LCx}, total capacitances for right (RCA), left anterior descending (LAD), and left circumflex (LCx) coronary arteries, respectively.